frontiers | Frontiers in Energy Research

TYPE Original Research
PUBLISHED 05 August 2022
DOI 10.3389/fenrg.2022.942314

OPEN ACCESS

EDITED BY
Juliusz Dąbrowa,
AGH University of Science and Technology, Poland

REVIEWED BY
Liangdong Fan,
Shenzhen University, China
Chi Zhang,
Wuyi University, China

*CORRESPONDENCE
Ben Breitung,
ben.breitung@kit.edu
Simon Schweidler,
simon.schweidler@kit.edu

†These authors have contributed equally to this work

SPECIALTY SECTION
This article was submitted to Electrochemical Energy Conversion and Storage,
a section of the journal
Frontiers in Energy Research

RECEIVED 12 May 2022
ACCEPTED 11 July 2022
PUBLISHED 05 August 2022

CITATION
Stenzel D, Zhou B, Okafor C, Kante MV, Lin L, Melinte G, Bergfeldt T, Botros M, Hahn H, Breitung B and Schweidler S (2022), High-entropy spinel-structure oxides as oxygen evolution reaction electrocatalyst.
Front. Energy Res. 10:942314.
doi: 10.3389/fenrg.2022.942314

High-entropy spinel-structure oxides as oxygen evolution reaction electrocatalyst

David Stenzel[1†], Bei Zhou[1†], Chukwudalu Okafor[2], Mohana Veeraju Kante[1], Ling Lin[1], Georgian Melinte[1,3], Thomas Bergfeldt[4], Miriam Botros[1], Horst Hahn[1,3,5], Ben Breitung[1*] and Simon Schweidler[1*]

[1]Institute of Nanotechnology, Karlsruhe Institute of Technology (KIT), Karlsruhe, Germany, [2]Department of Materials- and Geosciences, Technical University Darmstadt, Darmstadt, Germany, [3]Helmholtz Institute Ulm for Electrochemical Energy Storage, Ulm, Germany, [4]Institute for Applied Materials—Applied Materials Physics, Karlsruhe Institute of Technology (KIT), Karlsruhe, Germany, [5]Joint Research Laboratory Nanomaterials, Technical University Darmstadt, Darmstadt, Germany

High-entropy oxides are an upcoming research topic due to their broad range of possible crystal structures and applications. In this work, we want to present the change in the catalytic properties when using different elements to create a high-entropy spinel. Therefore, we used the nebulized-spray pyrolysis to synthesize the high-entropy spinel $(Mn_{0.2}Fe_{0.2}Ni_{0.2}Mg_{0.2}Zn_{0.2})_3O_4$ and later on exchanged the Mg or the Zn with elements with multiple possible oxidation states, in our example each with Cr or Co. The phase purity, morphology, microstructure and homogeneity were investigated by XRD, SEM and STEM-EDX. Their electrocatalytic performance and stability was measured *via* oxygen evolution reaction and cyclic voltammetry and compared to IrO_2, used as reference. The best performance of the synthesized materials was achieved by $(Mn_{0.2}Fe_{0.2}Ni_{0.2}Mg_{0.2}Cr_{0.2})_3O_4$.

KEYWORDS

high-entropy materials, high-entropy spinels, catalysis, oxygen evolution reaction, electrocatalyst, nebulized spray pyrolysis

Introduction

Due to today's demand for renewable energy sources and generation, many new technologies are becoming the focus of scientific interest. One of these promising technologies is the fuel cell, which uses hydrogen and oxygen to generate electricity and can be used in a variety of applications. However, if fuel cells are to be used on a potentially large scale, the supply of reactants must be ensured. One such option is electrolysis of water, the reverse process of the fuel cell, which uses an applied potential to split water into hydrogen and oxygen. When combined with renewable energy sources, such as coastal wind energy, it offers the possibility of forming large quantities of hydrogen and oxygen directly at energy generation sites. Unfortunately, the water-splitting reactions—$2O^{2-}$ are oxidized to O_2 at the anode and $2H^+$ are reduced to H_2 at the cathode—have a large overvoltage that results in wasted energy, since a much higher

amount of energy must be expended to split water than would theoretically be necessary. Therefore, catalyst materials that reduce the overvoltage of the water splitting reaction are under intense investigation (Lee et al., 2012; Katsounaros et al., 2014).

Here, we focus on catalysts for the oxygen evolution reaction (OER), the reaction in which oxygen is oxidized at the anode (Gray, 2009; Man et al., 2011; Katsounaros et al., 2014; Cherevko et al., 2016). State-of-the-art catalysts that exhibit excellent OER activity typically include noble metals and their oxides, e.g., Ir, IrO_2, Ru, and RuO_2. However, the drawbacks of noble metal oxides as OER catalysts are their high cost, scarcity, and poor long-term stability in alkaline electrolytes, which limit their large-scale applications (Lee et al., 2012; Cherevko et al., 2016). Therefore, it is important to develop new cost-effective and durable electrocatalysts with high catalytic activity, therefore much research has been done in this area (Trasatti, 1980; Man et al., 2011). Many different materials, structures, and catalyst types have been tested, metal oxides and sulfides, spinels and perovskites, homogeneous and heterogeneous catalysts, to name a few (Matsumoto and Sato, 1986; Sun and Dai, 2021).

A novel and promising approach to potentially high-performance catalysts is the use of high-entropy materials (HEMs) (Albedwawi et al., 2021; Sun and Dai, 2021). HEMs are a class of materials in which many different elements are incorporated into a single-phase crystal structure and often exhibit unexpected properties due to intrinsic elemental interactions. The original idea behind high-entropy materials was to produce materials with a very high configurational entropy (S_{config}), such that the absolute value of the entropy-dependent second term of the Gibbs-Helmholtz equation ($T\Delta S$) increases, potentially stabilizing the crystal structure. These special cases are called entropy-stabilized materials, but they represent only a small fraction of high-entropy materials because the energy conditions are rarely satisfied (Murty et al., 2019; Oses et al., 2020). In general, a material is called HEM, if S_{config} is greater than $1.5R$. The absolute value of S_{config} depends solely on the number of different elements and their stoichiometry (Supplementary Equation S1) (Murty et al., 2019). Therefore, it is necessary to incorporate a large number of elements (preferably equimolar) into a single-phase structure, resulting in different interactions between them; these interactions are called cocktail effects and are the basis for the unique properties of HEMs. Depending on the variation of the elements, the cocktail effects and thus the material properties can be tailored, and in some cases even properties that are not expected can be obtained. In the arsenal of material design, property control is fundamental and HEMs provide even more precise control by adding and/or subtracting elements, providing the ability to fine-tune the material (Oses et al., 2020; Ma et al., 2021). Due to the high-entropy configuration, which requires a homogeneous distribution of elements in the crystal structure and also on the surface of the materials, HEMs can behave completely differently in terms of catalytic properties than catalysts with surfaces made of binary materials (Pedersen et al., 2021). This is due to the high sensitivity to the chemical environment of the catalytic reactions that usually take place on the surface of a material. The unique surface of a HEM with atomic-sized catalytic centers and an elemental composition that may stabilize more than one transition state can be seen as the reason for a potential next-generation catalyst that expands the range from homogeneous to heterogeneous to high-entropy catalytic materials.

With HEMs, it is possible to vary the material composition and still maintain functionality. This makes it possible to minimize or avoid the use of rare or expensive elements. In particular, if noble metal catalysts such as RuO_2 and IrO_2 can be substituted for OER, this allows the development of very low-cost catalysts (Gray, 2009). So far, multiple different high-entropy alloys (HEA) combinations have been used as OER catalysts (Li and Chen, 2021; Li et al., 2021; Wang et al., 2021; You et al., 2022; Zhang et al., 2022). HEA catalysts show superior performance and increased stability compared to conventional binary or ternary alloys. These effects are most probably related to the entropy-driven structure stabilization and the associated effects among the incorporated metals (Ma et al., 2021). The same improvements are to be expected when comparing high-entropy oxides (HEOs), sulfides, etc. to their conventional binary or ternary forms. Several HEM materials have been investigated, e.g., high-entropy perovskites, high-entropy sulfides, and high-entropy spinels. Since they exhibit overpotential in the range of RuO_2 and/or IrO_2 for OER, further studies are encouraged (Albedwawi et al., 2021; Sun and Dai, 2021).

One of the first attempts to use HEOs as electrocatalysts was carried out by Wang et al. (2019) They used the high entropy spinel (HESp) $(CoCuFeMnNi)_3O_4$ for OER and achieved better OER activity than mixed metal oxides with fewer elements. The improved OER performance was attributed to the highly dispersed active sites, fast material diffusion, and excellent conductivity (Wang et al., 2019). Subsequently, various HEOs were used for OER (Jin et al., 2021; Nguyen et al., 2021; Yang et al., 2021).

Using the HESp $(Cr_{0.2}Mn_{0.2}Fe_{0.2}Co_{0.2}Ni_{0.2})_3O_4$ and various medium-entropy spinels, Sun et al. confirmed that the high entropy approach leads to a significant improvement in OER kinetics and higher stability in KOH solution than the comparable medium entropy materials, further validating the theory of Pedersen et al. (Pedersen et al., 2021; Sun et al., 2022). In addition, Einert et al. (2022) show that by changing the porosity of $(Cr_{0.2}Mn_{0.2}Fe_{0.2}Co_{0.2}Ni_{0.2})_3O_4$, the geometric current density can be significantly improved compared to dense samples. This indicates that spinel materials with high entropy are generally suitable as OER catalysts, but can be further optimized.

TABLE 1 Overview of the high-entropy spinel (HESp) materials.

Material	Structure formula
HESp1	$(Mn_{0.2}Fe_{0.2}Ni_{0.2}\mathbf{Mg}_{0.2}\mathbf{Zn}_{0.2})_3O_4$
HESp2	$(Mn_{0.2}Fe_{0.2}Ni_{0.2}\mathbf{Mg}_{0.2}\mathbf{Cr}_{0.2})_3O_4$
HESp3	$(Mn_{0.2}Fe_{0.2}Ni_{0.2}\mathbf{Mg}_{0.2}\mathbf{Co}_{0.2})_3O_4$
HESp4	$(Mn_{0.2}Fe_{0.2}Ni_{0.2}\mathbf{Cr}_{0.2}\mathbf{Zn}_{0.2})_3O_4$
HESp5	$(Mn_{0.2}Fe_{0.2}Ni_{0.2}\mathbf{Co}_{0.2}\mathbf{Zn}_{0.2})_3O_4$
HESp6	$(Mn_{0.2}Fe_{0.2}Ni_{0.2}\mathbf{Cr}_{0.2}\mathbf{Co}_{0.2})_3O_4$

In this report, we show that one possibility for further optimization is to modify the composition and property changes due to cocktail effects. These changes are investigated by synthesizing several HESps containing cheap and readily available transition metals and comparing their structural and OER properties. For this purpose, the elemental composition of the starting spinel $(Mn_{0.2}Fe_{0.2}Ni_{0.2}Mg_{0.2}Zn_{0.2})_3O_4$ is varied by replacing Mg and/or Zn with Co and/or Cr. The influence of the change is investigated by XRD, SEM, STEM-EDX and the analysis of the OER measurements.

Materials and methods

Synthesis: The HESps containing five transition metals were synthesized by nebulized spray pyrolysis (NSP) (Messing et al., 1993; Sarkar et al., 2017). First, 200 mL of a 0.1 M nitrate salt solution of the respective transition metals ($Mn(NO_3)_2{\cdot}6H_2O$ (abcr GmbH, Karlsruhe, Germany, 98%), $Fe(NO_3)_3{\cdot}9H_2O$ (abcr GmbH, Karlsruhe, Germany, 98%), $Ni(NO_3)_3{\cdot}6H_2O$ (abcr GmbH, Karlsruhe, Germany, 99.9%), $Cr(NO_3)_3{\cdot}9H_2O$ (abcr GmbH, Karlsruhe, Germany, 99%), $Co(NO_3)_2{\cdot}6H_2O$ (abcr GmbH, Karlsruhe, Germany, 99%), $Mg(NO_3)_3{\cdot}6H_2O$ (SigmaAldrich, St. Louis, MO, United States, 99%) and $Zn(NO_3)_2{\cdot}6H_2O$ (Riedel-de Haën, Seelze, Germany, 98%) were prepared. Subsequently, each homogenous clear aqueous solution was dispersed into fine droplets by a nebulizer. The resulting mist was passed through a hot-wall reactor at 1050°C using a carrier gas (N_2). The formed powder was collected on a filter paper in a heated collector at 120°C to prevent water vapor from condensing on the powders. The compositions can be seen in Table 1.

Material characterization: X-ray diffraction (XRD) patterns were collected on the as-synthesized powder samples, using a STOE Stadi P diffractometer, equipped with a Ga-jet X-ray source (Ga-Kβ radiation, 1.2079 Å). Patterns were collected between 10° and 90° 2Θ with a step size of 0.03° and a scanning rate of 0.36°/min. Rietveld refinement was performed by using TOPAS Academics V5 software. Scanning electron microscopy (SEM) imaging was done using a LEO-1530 electron microscope (Carl Zeiss AG, Oberkochen, Germany). The particle size distribution was evaluated using the image processing program ImageJ (Schneider et al., 2012). High resolution scanning transmission electron spectroscopy with energy-dispersive X-ray spectroscopy (STEM-EDX) measurements was performed on dry powder of the samples placed directly on the TEM holey carbon membrane without using solvents. Measurements were performed using a Themis300 electron microscope (Thermo Fischer Scientific, Eindhoven, Netherlands) working at 300 kV and equipped with a DCOR probe corrector (CEOS, Heidelberg, Germany) and a Super X EDX detector (Thermo Fischer Scientific, Eindhoven, Netherlands). Velox software was used to quantify the EDX data. The elemental maps are represented as net intensities of the selected energy lines. The elements were determined by optical emission spectrometry (ICP-OES, iCAP 7600DUO from ThermoFisher Scientific, Waltham, MA, United States). About 10 mg of the samples (weighing accuracy ± 0.04 mg) were dissolved in 6 mL hydrochloric acid, 2 ml nitric acid at 353 K for 4 h in a graphite oven (EasyDigest, Analab, Hoenheim, France). The analysis of the elements were accomplished with four different calibration solutions and an internal standard (Sc). The range of the calibration solutions did not exceed a decade. The two or three major wavelength of the elements has been used for calculation. The oxygen content was analyzed with the method of carrier gas hot extraction (CGHE). A commercial oxygen/nitrogen analyzer G8 Galileo (Bruker AXS, Karlsruhe, Germany) was used. The oxygen concentration was calibrated with TiO_2 (990001, Lot: 21919, Alpha, Kandel, Germany, 99,995%) and ZrO_2 (996001, Lot: 22317, Alpha, Kandel, Germany, 99,978%) and was verified with a NMC532 (LCM52318043, MTI Corp., Richmond, Californian, United States). The calibration range was close to the concentration of the samples. The standards and the samples were weighed in the range from about 2 mg (weighing accuracy ± 0.05 mg) in Sn crucibles (5–12 mm). The package was put into an outgassed (900 A) high temperature graphite crucible with about 150 mg graphite. The measurements take place at about 850 A. The evolving gas CO were swept out by helium as an inert carrier gas and measured by infrared detectors.

Electrochemical characterization: The electrocatalytic OER measurements were performed under ambient conditions with a constant temperature of 30°C using a modulated speed rotator (Equilabrium SAS, Lyon, France) and a biologic VSP potentiostat (BioLogic Sciences Instruments, Seyssinet-Pariset, France). A typical three-electrode system was assembled, using 1M potassium hydroxide (KOH) (reagent grade, Sigma Aldrich, Germany, 90%) solution as electrolyte, a rotating glass carbon electrode (0.196 cm^2) as working electrode, a Pt spiral as counter electrode, and an Ag/AgCl electrode as reference electrode. To prepare the working electrode, 10 mg active material, 100 µL Nafion (5 wt% Nafion in water/1-propanol, VWR International GmbH, Bruchsal, Germany), 100 µL ultra-pure water, produced and purified with a Millipore Milli-Q system (Merck KGaA,

Darmstadt, Germany), and 1800 µL 2-propanol (VWR, International GmbH, Germany, >99.9%) were mixed by an ultrasonic homogenizer (Scientz-IID, Ningbo Scientz Biotechnology Co., Ltd., Ningbo, Zhejiang, China) in an ice water bath for 30 min. For each measurement 8 µL of the solution was dropped on the working electrode and dried in air at room temperature. Before each measurement, 150 mL of the electrolyte in the electrochemical three electrode cell was saturated with N_2 for 30 min. Each measurement consists of two steps: (I) cyclic voltammetry (CV) containing two cycles between −0.8 and 0.3 V versus Ag/AgCl at 50 mV s^{-1} in N_2-saturated electrolyte and (II) after switching the gas flow to O_2 and waiting for 30 min to saturate the electrolyte, linear sweep voltammetry (LSV) was performed in the potential range from 0 to 1 V versus Ag/AgCl to measure the OER activity. IrO_2 (AlfaAesar, Kandel, Germany, 99%) was measured as reference material. The potential ($E_{Ag/AgCl}$) was calibrated with the reversible hydrogen electrode (RHE) potential E_{RHE} by using the equation $E_{RHE} = E_{Ag/AgCl} + 0.1919 + 0.059 * pH$. Tafel curves were obtained by plotting log I versus overpotential. The catalytic active area was determined by evaluating the second derivative of the curves.

CV measurements were performed to evaluate the long-term stability. One thousand CV cycles were applied to the electrode materials between 0.32 and 0.82 V versus Ag/AgCl at 50 mV s^{-1} in O_2-saturated electrolyte to observe the evolution of the current. Additionally, five hundred CV cycles were applied to the electrode materials between −0.8 and 0.3 V versus Ag/AgCl at 50 mV s^{-1} in N_2-saturated electrolyte to observe the material behavior in this voltage range. Electrochemical impedance spectroscopy (EIS) was measured between 1.4 and 1.8 V RHE versus open-circuit potential (OCP) and between 100 kHz and 100 mHz with AC modulation of 10 mV and 25 points per decade.

Results and discussion

The aim of this research was to investigate the catalytic properties of high-entropy spinels for the OER and to elaborate the role of different elements on the activity. Six different high-entropy compounds were synthesized, namely $(MnFeNiMgZn)_3O_4$ (HESp1), $(MnFeNiMgCr)_3O_4$ (HESp2), $(MnFeNiMgCo)_3O_4$ (HESp3), $(MnFeNiCrZn)_3O_4$ (HESp4), $(MnFeNiCoZn)_3O_4$ (HESp5) and $(MnFeNiCrCo)_3O_4$ (HESp6). Note that the last two elements in the brackets have been changed to produce different compositions, while Mn, Fe, and Ni are included in each material.

Based on Supplementary Equation S1, the S_{config} calculation for all HESp materials gave 1.61*R*, which makes them HEMs. Another condition is the equimolar ratio of the metal species and their homogeneous distribution, which will be discussed later. The general idea behind high-entropy materials is to produce multicomponent compounds that change their properties with respect to a desired characteristic related to their elemental composition and stoichiometry. By changing the composition or stoichiometry, the properties can be tailored and precisely adjusted. The changes that occur are related to the so-called "cocktail effects," which are interactions between elements that occur when different elements with different electronic states, electronegativities, ion sizes, preferred structures, oxidation states, etc., are mixed.

In order to evaluate the crystal structure and phase composition of the HESp materials XRD measurements and Rietveld refinement analysis were performed. A comparison of the obtained XRD patterns is displayed in Figure 1A. Figure 1B shows the exemplary Rietveld refinement of HESp1 and HESp6. With the exception of HESp6, which has a pure spinel structure (*Fd-3m, ICSD collection code: 12807*), all other HESp materials consist of a mixture of a spinel and a rock-salt structure (*Fm-3m, ICSD collection code: 9866*) (Figure 1 and Figure 2A).

The reason why different compositions have different phases after synthesis could be the following. The enthalpy of mixing indicates the energy required to mix the different elements. Only if the enthalpy of mixing is not too large, a single-phase structure can form. The differences in ionic radius and especially in oxidation state of the different incorporated elements play a crucial role in changing the enthalpy of mixing. If the size differences are too large or if internal redox reactions occur between the ions that make them incompatible for a particular structure, the enthalpy of mixing will be too large to form a stable single-phase compound. In addition, different synthesis methods may result in oxidation of the elements during synthesis, changing the intended average oxidation state during synthesis (e.g., an average oxidation state of 2+ is required to form a stable rock salt compound. If Fe^{2+} is oxidized to Fe^{3+} during synthesis, internal charge balance is required to maintain charge neutrality). Matching the synthesis conditions for all samples requires a number of further studies and is not easily achieved with NSP (Stygar et al., 2020). The lattice parameters of all materials can be found in Supplementary Table S1.

First, HESp1, HESp2, and HESp3 will be compared. Using HESp1 [$(MnFeNiMgZn)_3O_4$] as a starting material, it can be seen that the lattice parameters of both spinel and rock-salt phases increase when Zn is replaced by Cr or Co. This is remarkable because the ionic radius of Cr (0.615 Å) and Co (0.58 Å) in their 3+ or 2+ states is smaller than the radius of Zn^{2+} (Dai et al., 2021). Later, in HESp6, when both Cr and Co are incorporated into the spinel instead of Zn and Mg, the opposite trend, a decrease in lattice parameters, was observed. Moreover, for HESp2 and HESp3, the proportion of rock-salt phase increased from approximately 5% (HESp1) to 20% (Figure 2A). A comparable behavior was also observed for HESp4 and HESp5. In both cases, Mg was replaced by either Cr or Co compared to the initial material [HESp1, $(MnFeNiMgZn)_3O_4$], resulting in an increase in the lattice parameters. In both cases, the increase in the *a*-axis

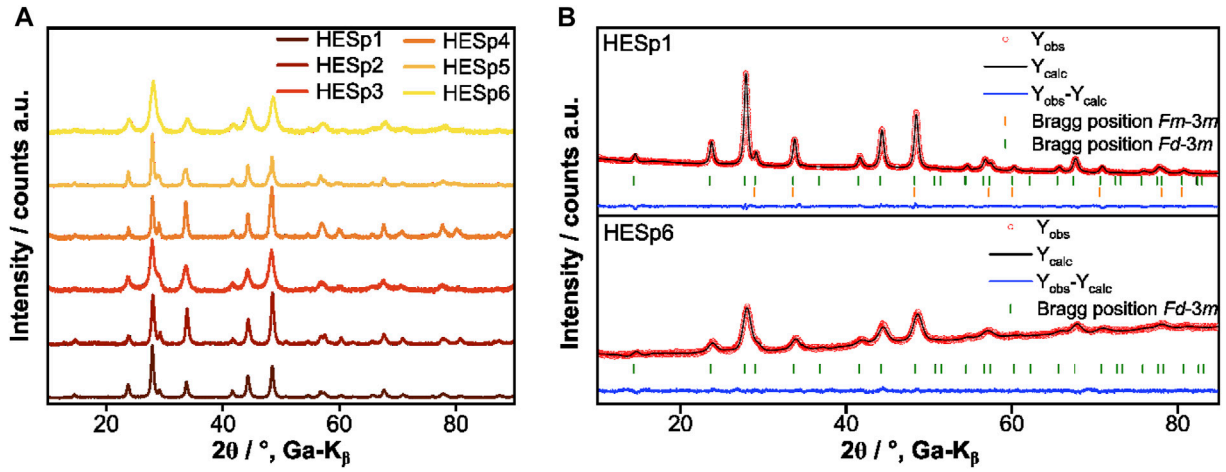

FIGURE 1
(A) Comparison of the normalized XRD patterns of the HESp materials synthesized *via* NSP. **(B)** Rietveld refinement of HESp1 and HESp6.

was larger than for HESp2 and HESp3, which can be probably attributed to the larger ionic radius of Zn (0.6 Å) compared to Mg (0.57 Å) (Figure 2B). The percentage of rock-salt phases was ~27 and ~23% for HESp3 and HESp4, respectively. The only exception was HESp6, which exhibited a single phase spinel structure. The lattice constants of HESp6 are the smallest at ~8.43 Å and show a different trend from the lattice expansion when Zn is replaced in HESp2 and HESp3, as explained above. The lack of rock-salt structure could be due to the fact that Cr and Co, unlike Zn and Mg, are free to choose their oxidation state and are therefore not subject to any restriction, which may lead to charge balance and thus preferential spinel structure formation. This could also be one of the reasons why all materials containing either Zn or Mg, or both, exhibit an additional rock-salt structure. A similar observation was made by Wang et al. (2020) during the stepwise addition of Li to the spinel-like materials $(NiFeMnCrMg)_3O_4$, $(NiFeMnZnMg)_3O_4$, and $(NiFeMnCrCo)_3O_4$. As the content of monovalent Li^+ ions increased, a transformation from the spinel to the rock-salt phase occurred because, above a certain Li content, charge balance by oxidation of the other transition metals was no longer possible, resulting in the formation of a rock-salt structure with a lower O:M ratio to compensate for the lack of positive charges. It can therefore be assumed that similar behavior also occurs in HESp materials. The ionic radii of the divalent and trivalent ions in tetrahedral coordination are Zn^{2+}: 60 p.m., Co^{2+}: 58 p.m., and in octahedral coordination Zn^{2+}: 74 p.m., Co^{2+}: 65–74.5 p.m. (ls-hs), Co^{3+}: 54.5–61 p.m. (ls-hs), Co^{3+}: 54.5–61 p.m. (ls-hs) Cr^{3+}: 61.5 p.m. (Shannon, 1976). In a normal spinel structure AB_2O_4 the A cations occupy tetrahedral sites while the B cations octahedral sites, in an inverse spinel half of the B cations replace the A cations in tetrahedral positions while the A cations move to octahedral positions. If the high-entropy compounds are normal or inverse spinels, cannot be predicted.

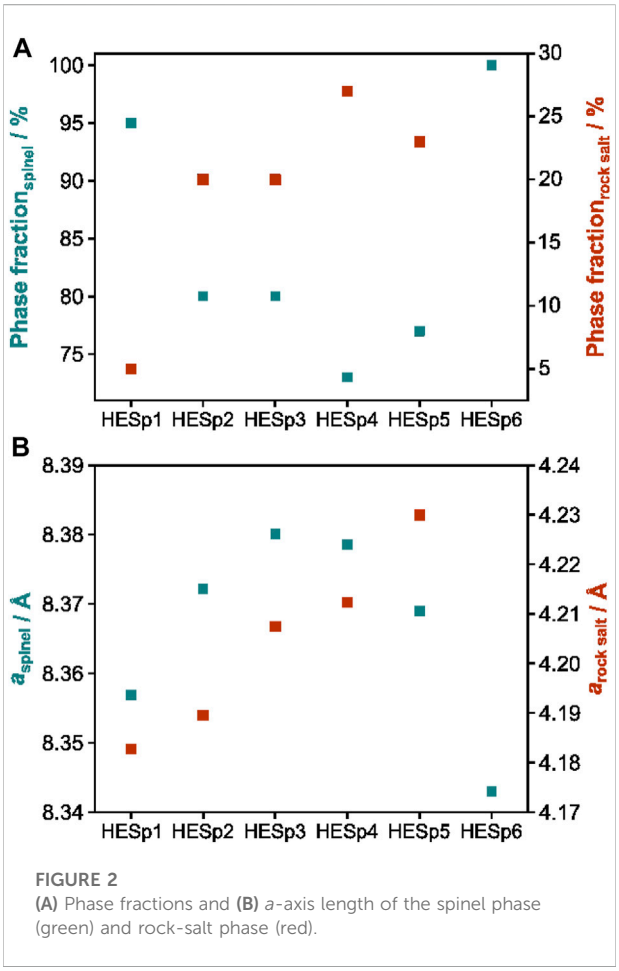

FIGURE 2
(A) Phase fractions and **(B)** *a*-axis length of the spinel phase (green) and rock-salt phase (red).

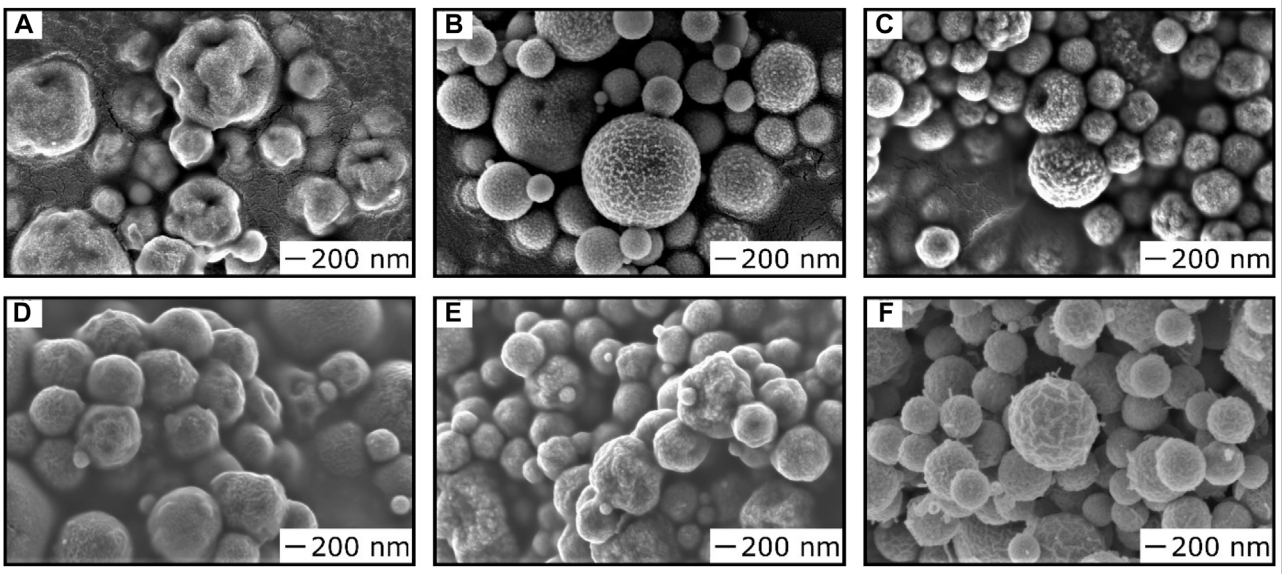

FIGURE 3
(A–F) Top-view SEM images of HESp1-6 prepared by NSP.

The morphology of the HESp materials prepared with NSP was studied by SEM (Figure 3). They are composed of hollow and filled spheres, and the size of most particles ranges from 0.2 to 1.2 µm. Optical analysis of the size distribution shows that the diameters vary between 100 nm and 2 µm (Supplementary Figure S1) (Schneider et al., 2012). The average particle size of $(MnFeNiMgCr)_3O_4$ is about 0.5 µm, and almost 70% of the particles are in the size range between 200 and 600 nm. It can be concluded that only 8.4% of the particles are larger than 1 µm, as shown in the particle size distribution diagram (Supplementary Figure S1).

The spheres of the different materials have different surface structures: more or less round, concave, notched, some smooth and some rough. SEM images of HESp samples at a different magnification are shown in Supplementary Figure S2. The particles without Zn have a more compact and round shape (Figures 3B,C,F). This can be attributed to the different solute precipitation rates at the surface and in the center, which are due to the different solubilities of the starting materials and the evaporation rates of the solvents (Messing et al., 1993; Shih et al., 2012). During the cooling stage, the oxide shell with different particle sizes can show different deformation behavior, resulting in smooth or uneven surfaces. In conjunction with the morphology analysis of the other five samples, it can be deduced that all HESp powders with different components are distributed in the same size range (Table 2). SEM images of the reference catalyst IrO_2 show micrometer-sized, angular crystals aggregating into clusters (Supplementary Figure S3). ICP measurement were performed to analyze the exact chemical formula (Table 2). All compounds show a nearly equimolar distribution of the elements further confirming their status as HEMs.

TABLE 2 Overview of the formula based on ICP and the average particle size of the HESp materials.

Material	Structure formula	$\bar{d}$/µm
HESp1	$(Mn_{0.19}Fe_{0.19}Ni_{0.19}Zn_{0.18}Mg_{0.19})_3O_4$	0.460
HESp2	$(Mn_{0.19}Fe_{0.19}Ni_{0.2}Cr_{0.19}Mg_{0.19})_3O_4$	0.485
HESp3	$(Mn_{0.2}Fe_{0.2}Ni_{0.2}Co_{0.2}Mg_{0.19})_3O_4$	0.406
HESp4	$(Mn_{0.19}Fe_{0.19}Ni_{0.19}Cr_{0.18}Zn_{0.18})_3O_4$	0.483
HESp5	$(Mn_{0.2}Fe_{0.19}Ni_{0.19}Co_{0.19}Zn_{0.19})_3O_4$	0.473
HESp6	$(Mn_{0.19}Fe_{0.19}Ni_{0.19}Cr_{0.18}Co_{0.19})_3O_4$	0.463

STEM-EDX was used to investigate the element distribution. Figure 4 shows that all elements in the exemplary HESp2 are uniformly distributed. No segregation of individual elements was detected, leading to the assumption that a homogeneous distribution of elements also exists within the rock-salt phase detected by XRD. Based on that and the distribution seen in Table 2 the requirements for a high-entropy materials as given in Supplementary Equation S1 are fulfilled.

The catalytic performance of the materials for the OER reaction was tested by preparing a glassy carbon working electrode covered with a 2-propanol-based solution of the respective catalyst active material and Nafion. Initial CV steps before OER are performed to activate the material. Figure 5A shows the behavior of the synthesized HESps and the reference material IrO_2 during OER. All measurements were performed

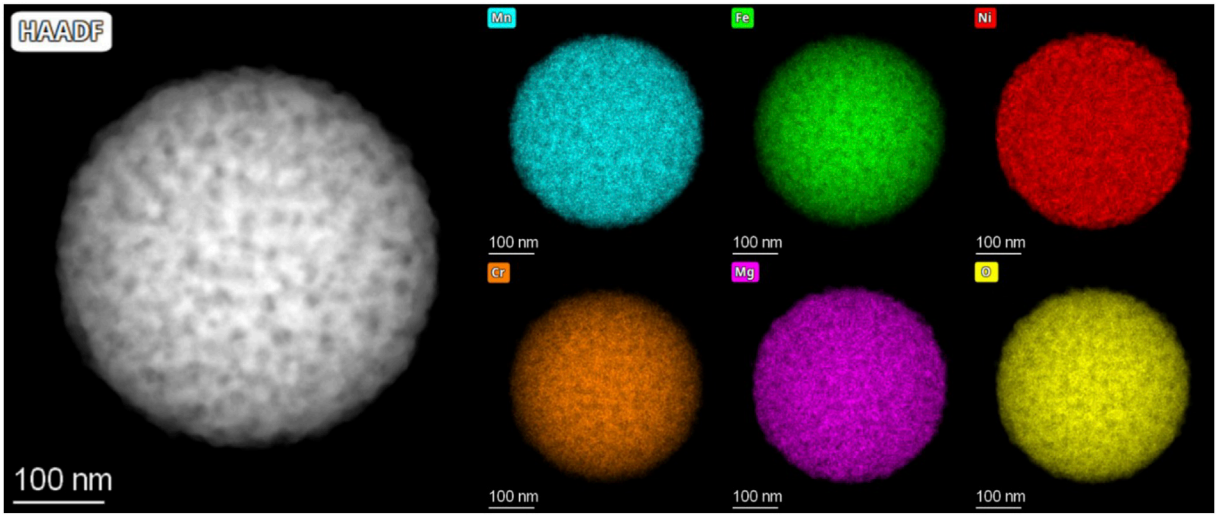

FIGURE 4
STEM-EDX mapping of HESp2. All elements are distributed uniformly.

during constant O_2 flow and are normalized to the geometric electrode surface. To avoid interference from O_2 bubbling, the upper applied potential was fixed at 1.8 V versus RHE. This procedure allows to observe the initial potential of the OER, the overpotential at 10 and 50 mA/cm^2, and to compare the reaction kinetics based on the Tafel slope of the curve.

The differences in the electrocatalytic potential of all materials can be seen in the differences between the OER onsets at 0.5 mA/cm^2 and the overpotentials (Figure 5C). IrO_2 as a reference material has a higher value than most HESp materials with an OER onset of 1.51 V vs. RHE. Only HESp4 shows a higher onset of 1.52 V versus RHE. For the calculation of the overpotential, the potential difference between the potential of each HESp material at 10 and 50 mA/cm^2 and the equilibrium potential for oxygen reduction at 1.23 V was calculated (Supplementary Table S2) (Kulkarni et al., 2018). All HESp materials showed lower overpotentials at 10 mA/cm^2 compared to IrO_2. Whereby HESp2 and HESp3 exhibited the lowest overvoltage values at 10 mA/cm^2 with approximately 290 and 306 mV. Whereas the values of overpotential at 50 mA/cm^2 of HESp1, HESp2, HESp3, and HESp5 are all located close to each other in a range of ~ 490–540 mV. For HESp4, HESp6, and IrO_2 an overpotential could not be detected at 50 mA/cm^2. The catalytic activities of the HESp materials and the reference material (IrO_2) were determined by the evaluation of the Tafel slope (Figure 5B). The Tafel slopes were obtained from LSV curves collected (Figure 5A). In addition to the smallest onset potentials and overpotentials, HESp1, HESp2, and HESp3 also exhibit the smallest Tafel slopes with 35.5, 46.5, and 45.9 mV dec^{-1}, respectively, which are all lower than IrO_2 with 49.5 mV dec^{-1}. Generally, a lower Tafel slope indicates easier acceleration of electron transfer and migration during the catalytic process, allowing the catalyst to produce larger current densities at the same potential.

Compared to literature values, the HESp materials show good performances. Sun et al. and Einert et al. performed OER measurements on similar materials and reported overpotentials of around 320 mV at 10 mA/cm^2 and a Tafel slope of 54.5 mV/dec^{-1} (Sun et al., 2022)· (Sun et al., 2018), or for mesoporous materials an overpotential of 350 mV at 10 mA/cm^2 and a Tafel slope of 35.0 mV dec^{-1}. The best performing materials with regard to overpotential at 10 mA/cm^2 and Tafel slope in this report were HESp2 and HESp1, which reveal an overpotential of 290 mV and a Tafel slope of 46.5 (HESp2) or an overpotential of 346 mV and a Tafel slope of 35.5 mV dec^{-1}, respectively (Einert et al., 2022).

To further asses the electrochemical activity of HESp2, repeated CV measurements in O_2 saturated electrolyte were performed in the OER range between 1.3 and 1.8 V vs. RHE. (Figure 5D). This procedure allows to study the aging of the catalyst during long-term CV-tests. 1000 cycles were performed on the material between 1.3 and 1.8 V versus RHE in 1 M KOH at 50 mV s^{-1} in O_2-saturated electrolyte to observe the evolution of the current. From the first cycle up to cycle 100 in Figure 5D, an increase of the final current at 1.8 V vs. RHE is visible with a big step between cycle one and cycle 25, followed by a small step until cycle 50 and a minuscule one until cycle 100. The corresponding values for cycle one, two, 25, 50, and 100 are 3.5, 4.5, 12.1, 13.7, and 14.0 mA cm^{-2}. Up to cycle 1000 the current decreases up to 4.1 mA cm^{-2}, whereas the loose for each cycle get smaller again with increasing cycle number. The increase in the beginning can be associated to the missing activation of the material *via* CV

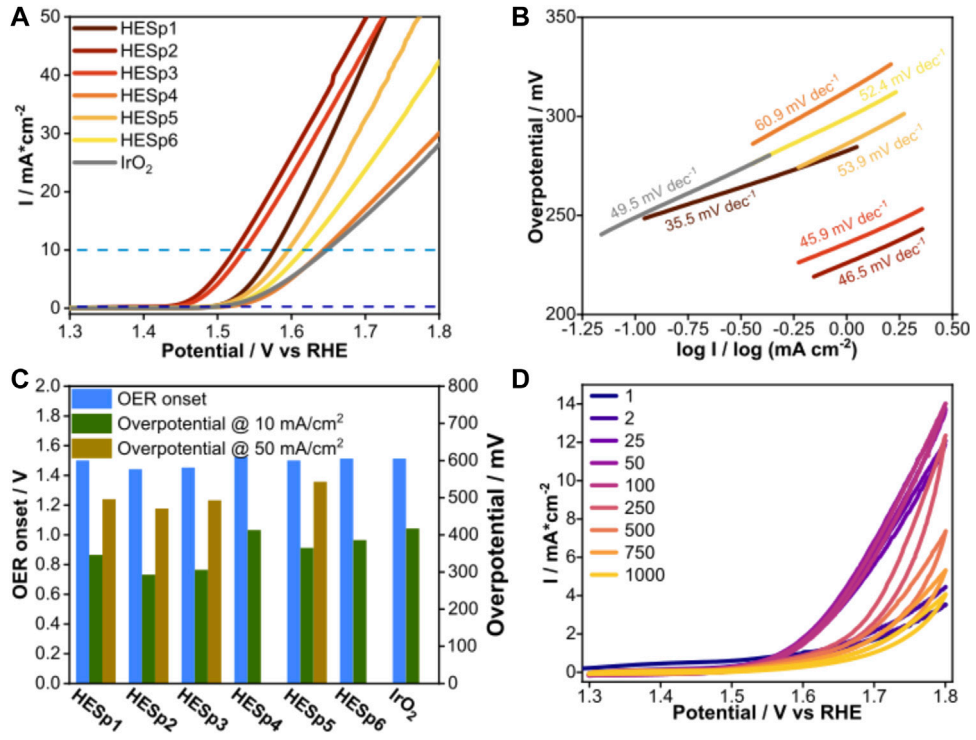

FIGURE 5
(A) LSV curves of the different HESp materials including IrO_2 during the OER in O_2-saturated 1 M KOH, the dotted lines mark the values for the OER onset (dark blue) and overpotential at 10 mA/cm^2 (light blue). **(B)** Tafel slopes of the different HESp materials. **(C)** Comparison of the values for OER onset and overpotentials. Missing bars indicate a very large overpotential. **(D)** Voltammogram of HESp2 during CV after 1, 2, 25, 50, 100, 250, 500, and 1,000 cycles.

before starting the CV measurements compared to the LSV measurement (Shinagawa et al., 2017; Liu et al., 2020). The decrease shows signs of material failure due to decomposition processes.

Electrochemical impedance spectroscopy (EIS) was measured between 1.4 and 1.8 V RHE versus open-circuit potential (OCP) and between 100 kHz and 100 mHz with AC modulation of 10 mV and 25 points per decade.

The Nyquist plots of HESp2 and IrO_2 measured between 1.4 and 1.8 V RHE and OCP are shown in Supplementary Figure S4. This range was chosen because of the onset of the catalytic reaction (Figure 5D). Both materials show only a semicircle, so it can be confirmed that only one charge transfer driven reaction takes place at some kind of catalytically active surface. The mixture of rock-salt and spinel phases in HESp2 has no significant effect on this reaction. IrO_2 exhibits much lower charge transfer resistance compared to HESp2 at any potential (Supplementary Figure S4B). Therefore, a higher catalytic activity of IrO_2 compared to HESp2 would be expected due to faster kinetics. However, the opposite was observed. The difference is probably influenced by the differences in morphology. This indicates that the OER performance of the HESp materials might be still underestimated due to the non-optimized surface area and composition. A quantitative comparison of EIS measurements between materials with such different powder morphologies is very difficult.

Looking at the elemental composition of the HESp materials, it can be seen that all Mg-containing materials (HESp1, HESp2, and HESp3) have the best catalytic OER properties. However, by replacing Zn (in HESp1) with Cr (HESp2) or Co (HESp3), the catalytic properties were further improved. Consequently, it can be assumed that Mg has a positive and Zn probably a lesser impact on the OER performance. This assumption is further strengthened by the fact that in the materials in which Mg was exchanged for Cr (HESp4) or Co (HESp5) and the Zn content was maintained, as well as for HESp6 in which both Zn and Mg were exchanged for Cr and Co, all three combinations showed poorer catalytic properties. In the following, the effects of Mg, Cr, and Co on the OER performance are discussed in more detail. First, HESp1, HESp2, and HESp3 are compared, where the addition of Mg improves the OER performance, most probably, by changing the

electronic structure and optimizing the arrangement of surface atoms (Li et al., 2020). In addition to the influence of Mg, HESp2 obtains its improved electrocatalytic activity/potential for OER from the addition of Cr (Li et al., 2018; Shao et al., 2019). Dang et al. (2021) formulated that Cr atoms in the host matrix can modulate the electronic structure of the catalyst to achieve the optimal binding energies for oxygen intermediates with an enhanced charge/mass transfer process for the fast kinetics of OER reactions. Co oxides with a spinel structure generally exhibit good OER properties (Bergmann et al., 2015; Chen et al., 2015; Xu et al., 2019). Saddeler et al. describes the effect of adding Co to Fe_3O_4, which comes into play in HESp3, where Co improves OER reaction kinetics (Saddeler et al., 2021). The difference between HESp2 and HESp3 results from a stronger effect of Cr than of Co. HESp1 with Zn appears to be initially worse than HESp2 and HESp3. However it later reaches comparable values to HESp3. The reason for this, and thus the effect of Zn on our materials, cannot be clearly determined (Petrykin et al., 2011; Liu et al., 2014; Rebekah et al., 2020). Without Mg, the electrocatalytic performance is much lower in HESp4, HESp5, and HESp6. The combination of Co and Zn in HESp5 shows the best potential without Mg, which is due to the structural change of the surface and the higher density of accessible active Co^{3+} sites due to the incorporation of Zn^{2+} (Petrykin et al., 2011). HESp5 has comparable results to the $Zn_xCo_{3-x}O_4$ spinel, as shown by Liu et al. (2014). HESp6 with Co and Cr gives better results than HESp4 with Cr and Zn. The addition of Co increases the catalytic potential in HESp5 and HESp6 more than Cr in HESp6 and HESp4. Moreover, the electrocatalytic activity of the materials seems to be mainly influenced by the cocktail effect, which is based on the elemental composition rather than the crystal structure. In summary, the improvement of OER activities by the different compositions can be verified by the data available in the literature. The same applies to the influence of particle morphology in Figure 3. In addition, it should be mentioned at this point that the formation of the rock-salt type structure could also have an influence on the OER performance. It could be that catalytic OER is favored when the proportion of rock-salt structure increases, as is the case for HESp1 to HESP2 and HESp3, and that a further increase, as is the case for HESp4 and HESp5, in turn has a negative effect on catalytic activities. Further studies (e.g., DFT) could shed light on this, however, this is out of the scope of this study.

HEMs are considered to be very special catalytic materials. They can be seen as the next step in the chain from homogeneous to heterogeneous to high-entropy catalysts. The unique surface makes high-entropy materials very special because statistically distributed atomic size elements serve as catalytic centers. The diversity of elements might allow different transition states to be stabilized during the catalytic process, and their atomic distribution brings them into very close proximity to each other. Doping a homogenous catalyst could also change the electronic structure, but replacing an element in a high-entropy material would change all of the above effects. Furthermore, cocktail effects even add more complexity by granting each material composition a unique "fingerprint" that has great impact on the materials properties.

Conclusion

Six equiatomic high-entropy spinel materials, some with a high-entropy rock-salt type phase, were synthesized by the nebulized spray pyrolysis technique and investigated for their structural and electrocatalytic properties. All synthesized materials exhibit an average particle size between 0.4 and 0.5 μm, a uniform distribution of elements, and an equimolar ratio. Their electrocatalytic properties were compared with those of IrO_2, a commonly used catalytic material. The OER onset, overvoltage and Tafel slope of all synthesized materials give better values than IrO_2. $(Mn_{0.2}Fe_{0.2}Ni_{0.2}Mg_{0.2}Cr_{0.2})_3O_4$ obtained the best electrocatalytic properties with an OER onset of 1.44 V, overpotential of 293 mV (at 10 mA/cm^2) and Tafel slope of 46.5 mV dec^{-1}, closely followed by $(Mn_{0.2}Fe_{0.2}Ni_{0.2}Mg_{0.2}Co_{0.2})_3O_4$. An improvement in electrocatalytic performance with the addition of Mg is clearly evident. In general, this study shows that the incorporation of the high-entropy concept and thus the cocktail effect is a good way to develop a future-proof OER catalyst material.

Data availability statement

The raw data supporting the conclusions of this article will be made available by the authors, without undue reservation.

Author contributions

DS and BZ conducted the experiments, evaluated the data and co-wrote the manuscript. CO and LL conducted OER experiments. MK and GM performed SEM and TEM experiments, respectively. TB performed ICP-OES measurements. HH, BB, and SS co-wrote the manuscript, planned the experiments and did project administration. MB performed and evaluated EIS measurements.

Author contributions

All authors listed have made a substantial, direct, and intellectual contribution to the work and approved it for publication.

Funding

DS, BB, SS, MB, and HH acknowledge the support from EnABLES and EPISTORE, projects funded by the European Union's Horizon 2020 research and innovation program under grant agreement no. 730957 and 101017709, respectively. HH acknowledges financial support from the Deutsch Forschungsgemeinschaft (DFG) project HA 1344/43-1.

Conflict of interest

The authors declare that the research was conducted in the absence of any commercial or financial relationships that could be construed as a potential conflict of interest.

Publisher's note

Supplementary material

The Supplementary Material for this article can be found online at: https://www.frontiersin.org/articles/10.3389/fenrg.2022.942314/full#supplementary-material

References

Albedwawi, S. H., AlJaberi, A., Haidemenopoulos, G. N., and Polychronopoulou, K. (2021). High entropy oxides-exploring a paradigm of promising catalysts: A review. *Mat. Des.* 202, 109534. doi:10.1016/j.matdes.2021.109534

Bergmann, A., Martinez-Moreno, E., Teschner, D., Chernev, P., Gliech, M., De Araújo, J. F., et al. (2015). Reversible amorphization and the catalytically active state of crystalline Co3O4 during oxygen evolution. *Nat. Commun.* 6, 8625. doi:10.1038/ncomms9625

Chen, Z., Kronawitter, C. X., and Koel, B. E. (2015). Facet-dependent activity and stability of Co3O4 nanocrystals towards the oxygen evolution reaction. *Phys. Chem. Chem. Phys.* 17 (43), 29387–29393. doi:10.1039/c5cp02876k

Cherevko, S., Geiger, S., Kasian, O., Kulyk, N., Grote, J. P., Savan, A., et al. (2016). Oxygen and hydrogen evolution reactions on Ru, RuO2, Ir, and IrO2 thin film electrodes in acidic and alkaline electrolytes: A comparative study on activity and stability. *Catal. Today* 262, 170–180. doi:10.1016/j.cattod.2015.08.014

Dai, S., Li, M., Wang, X., Zhu, H., Zhao, Y., Wu, Z., et al. (2021). Fabrication and magnetic property of novel (Co, Zn, Fe, Mn, Ni)3O4 high-entropy spinel oxide. *J. Magn. Magn. Mat.* 536, 168123. doi:10.1016/J.JMMM.2021.168123

Dang, N. K., Tiwari, J. N., Sultan, S., Meena, A., and Kim, K. S. (2021). Multi-site catalyst derived from Cr atoms-substituted CoFe nanoparticles for high-performance oxygen evolution activity. *Chem. Eng. J.* 404, 126513. doi:10.1016/j.cej.2020.126513

Einert, M., Mellin, M., Bahadorani, N., Dietz, C., Lauterbach, S., Hofmann, J. P., et al. (2022). Mesoporous high-entropy oxide thin films: Electrocatalytic water oxidation on high-surface-area spinel (Cr 0.2 Mn 0.2 Fe 0.2 Co 0.2 Ni 0.2) 3 O 4 electrodes. *ACS Appl. Energy Mat.* 5, 717–730. doi:10.1021/acsaem.1c03190

Gray, H. B. (2009). Powering the planet with solar fuel. *Nat. Chem.* 1 (1), 7. doi:10.1038/nchem.141

Jin, Z., Lyu, J., Zhao, Y. L., Li, H., Chen, Z., Lin, X., et al. (2021). Top-down synthesis of noble metal particles on high-entropy oxide supports for electrocatalysis. *Chem. Mat.* 33 (5), 1771–1780. doi:10.1021/acs.chemmater.0c04695

Katsounaros, I., Cherevko, S., Zeradjanin, A. R., and Mayrhofer, K. J. J. (2014). Oxygen electrochemistry as a cornerstone for sustainable energy conversion. *Angew. Chem. Int. Ed.* 53 (1), 102–121. doi:10.1002/anie.201306588

Kulkarni, A., Siahrostami, S., Patel, A., and Nørskov, J. K. (2018). Understanding catalytic activity trends in the oxygen reduction reaction. *Chem. Rev.* 118 (5), 2302–2312. doi:10.1021/acs.chemrev.7b00488

Lee, Y., Suntivich, J., May, K. J., Perry, E. E., and Shao-Horn, Y. (2012). Synthesis and activities of rutile IrO 2 and RuO 2 nanoparticles for oxygen evolution in acid and alkaline solutions. *J. Phys. Chem. Lett.* 3 (3), 399–404. doi:10.1021/jz2016507

Li, H., Lai, J., Li, Z., and Wang, L. (2021). Multi-sites electrocatalysis in high-entropy alloys. *Adv. Funct. Mat.* 31 (47), 2106715. doi:10.1002/ADFM.202106715

Li, H., Sun, S., Xi, S., Chen, Y., Wang, T., Du, Y., et al. (2018). Metal–oxygen hybridization determined activity in spinel-based oxygen evolution catalysts: A case study of $ZnFe_{2-x}Cr_xO_4$. *Chem. Mat.* 30 (19), 6839–6848. doi:10.1021/acs.chemmater.8b02871

Li, K., and Chen, W. (2021). Recent progress in high-entropy alloys for catalysts: Synthesis, applications, and prospects. *Mat. Today Energy* 20, 100638. doi:10.1016/J.MTENER.2021.100638

Li, Z., Wang, S., Tian, Y., Li, B., Yan, H. J., Zhang, S., et al. (2020). Mg-doping improves the performance of Ru-based electrocatalysts for the acidic oxygen evolution reaction. *Chem. Commun.* 56 (11), 1749–1752. doi:10.1039/c9cc09613b

Liu, S., Zhang, J., Wang, H., Asefa, T., and Huang, X. (2020). A facile route to efficient water oxidation electrodes via electrochemical activation of iron in nickel sulfate solution. *ACS Sustain. Chem. Eng.* 8 (41), 15550–15559. doi:10.1021/acssuschemeng.0c04666

Liu, X., Chang, Z., Luo, L., Xu, T., Lei, X., Liu, J., et al. (2014). Hierarchical $Zn_xCo_{3-x}O_4$ nanoarrays with high activity for electrocatalytic oxygen evolution. *Chem. Mat.* 26 (5), 1889–1895. doi:10.1021/cm4040903

Ma, Y., Ma, Y., Wang, Q., Schweidler, S., Botros, M., Fu, T., et al. (2021). High-entropy energy materials: Challenges and new opportunities. *Energy Environ. Sci.* 14, 2883–2905. doi:10.1039/d1ee00505g

Man, I. C., Su, H. Y., Calle-Vallejo, F., Hansen, H. A., Martínez, J. I., Inoglu, N. G., et al. (2011). Universality in oxygen evolution electrocatalysis on oxide surfaces. *ChemCatChem* 3 (7), 1159–1165. doi:10.1002/cctc.201000397

Matsumoto, Y., and Sato, E. (1986). Electrocatalytic properties of transition metal oxides for oxygen evolution reaction. *Mat. Chem. Phys.* 14 (5), 397–426. doi:10.1016/0254-0584(86)90045-3

Messing, G. L., Zhang, S.-C., and Jayanthi, G. V. (1993). Ceramic powder synthesis by spray pyrolysis. *J. Am. Ceram. Soc.* 76 (11), 2707–2726. doi:10.1111/j.1151-2916.1993.tb04007.x

Murty, B. S., Yeh, J. W., Ranganathan, S., and Bhattacharjee, P. P. (2019). *High-entropy alloys*. 2nd ed. Netherlands: Elsevier Science.

Nguyen, T. X., Liao, Y. C., Lin, C. C., Su, Y. H., and Ting, J. M. (2021). Advanced high entropy perovskite oxide electrocatalyst for oxygen evolution reaction. *Adv. Funct. Mat.* 31 (27), 2101632. doi:10.1002/adfm.202101632

Oses, C., Toher, C., and Curtarolo, S. (2020). High-entropy ceramics. *Nat. Rev. Mat.* 5 (4), 295–309. doi:10.1038/s41578-019-0170-8

Pedersen, J. K., Batchelor, T. A. A., Yan, D., Skjegstad, L. E. J., and Rossmeisl, J. (2021). Surface electrocatalysis on high-entropy alloys. *Curr. Opin. Electrochem.* 26, 100651. doi:10.1016/j.coelec.2020.100651

Petrykin, V., MacOunova, K., Franc, J., Shlyakhtin, O., Klementova, M., Mukerjee, S., et al. (2011). Zn-doped RuO2 electrocatalyts for selective oxygen evolution: Relationship between local structure and electrocatalytic behavior in chloride containing media. *Chem. Mat.* 23 (2), 200–207. doi:10.1021/cm1028782

Rebekah, A., Anantharaj, S., Viswanthan, C., and Ponpandian, N. (2020). Zn-substituted MnCo2O4 nanostructure anchored over RGO for boosting the electrocatalytic performance towards methanol oxidation and oxygen evolution reaction (OER). *Int. J. Hydrogen Energy* 45 (29), 14713–14727. doi:10.1016/j.ijhydene.2020.03.231

Saddeler, S., Bendt, G., Salamon, S., Haase, F. T., Landers, J., Timoshenko, J., et al. (2021). Influence of the cobalt content in cobalt iron oxides on the electrocatalytic OER activity. *J. Mat. Chem. A* 9 (45), 25381–25390. doi:10.1039/d1ta06568h

Sarkar, A., Djenadic, R., Usharani, N. J., Sanghvi, K. P., Chakravadhanula, V. S. K., Gandhi, A. S., et al. (2017). Nanocrystalline multicomponent entropy stabilised transition metal oxides. *J. Eur. Ceram. Soc.* 37 (2), 747–754. doi:10.1016/j.jeurceramsoc.2016.09.018

Schneider, C. A., Rasband, W. S., and Eliceiri, K. W. (2012). NIH image to ImageJ: 25 Years of image analysis. *Nat. Methods* 9 (7), 671–675. doi:10.1038/nmeth.2089

Shao, C., Zhang, F., Li, X., Zhang, J., Jiang, Y., Cheng, H., et al. (2019). Influence of Cr doping on the oxygen evolution potential of SnO2/Ti and Sb-SnO2/Ti electrodes. *J. Electroanal. Chem. (Lausanne).* 832, 436–443. doi:10.1016/j.jelechem.2018.11.058

Shih, S. J., Wu, Y. Y., Chen, C. Y., and Yu, C. Y. (2012). Morphology and formation mechanism of ceria nanoparticles by spray pyrolysis. *J. Nanopart. Res.* 14 (5), 879. doi:10.1007/s11051-012-0879-4

Shinagawa, T., Ng, M. T. K., and Takanabe, K. (2017). Boosting the performance of the nickel anode in the oxygen evolution reaction by simple electrochemical activation. *Angew. Chem. Int. Ed.* 56 (18), 5061–5065. doi:10.1002/anie.201701642

Stygar, M., Dąbrowa, J., Moździerz, M., Zajusz, M., Skubida, W., Mroczka, K., et al. (2020). Formation and properties of high entropy oxides in Co-Cr-Fe-Mg-Mn-Ni-O system: Novel (Cr, Fe, Mg, Mn, Ni)3O4 and (Co, Cr, Fe, Mg, Mn)3O4 high entropy spinels. *J. Eur. Ceram. Soc.* 40 (4), 1644–1650. doi:10.1016/j.jeurceramsoc.2019.11.030

Sun, S., Li, H., and Xu, Z. J. (2018). Impact of surface area in evaluation of catalyst activity. *Joule* 2 (6), 1024–1027. doi:10.1016/j.joule.2018.05.003

Sun, Y., and Dai, S. (2021). High-entropy materials for catalysis: A new frontier. *Sci. Adv.* 7 (20), eabg1600. doi:10.1126/sciadv.abg1600

Sun, Z., Zhao, Y., Sun, C., Ni, Q., Wang, C., Jin, H., et al. (2022). High entropy spinel-structure oxide for electrochemical application. *Chem. Eng. J.* 431, 133448. doi:10.1016/j.cej.2021.133448

Shannon, R. D. (1976). Revised effective ionic radii and systematic studies of interatomic distances in halides and chalcogenides. *Acta Cryst. Sect. A* 32 (5), 751–767. doi:10.1107/S0567739476001551

Trasatti, S. (1980). Electrocatalysis by oxides - attempt at a unifying approach. *J. Electroanal. Chem. Interfacial Electrochem.* 111 (1), 125–131. doi:10.1016/S0022-0728(80)80084-2

Wang, D., Liu, Z., Du, S., Zhang, Y., Li, H., Xiao, Z., et al. (2019). Low-temperature synthesis of small-sized high-entropy oxides for water oxidation. *J. Mat. Chem. A* 7 (42), 24211–24216. doi:10.1039/c9ta08740k

Wang, J., Stenzel, D., Azmi, R., Najib, S., Wang, K., Jeong, J., et al. (2020). Spinel to rock-salt transformation in high entropy oxides with Li incorporation. *Electrochem* 1 (1), 60–74. doi:10.3390/electrochem1010007

Wang, X., Guo, W., and Fu, Y. (2021). High-entropy alloys: Emerging materials for advanced functional applications. *J. Mat. Chem. A* 9 (2), 663–701. doi:10.1039/d0ta09601f

Xu, Y., Zhang, F., Sheng, T., Ye, T., Yi, D., Yang, Y., et al. (2019). Clarifying the controversial catalytic active sites of Co3O4 for the oxygen evolution reaction. *J. Mat. Chem. A* 7 (40), 23191–23198. doi:10.1039/c9ta08379k

Yang, J. X., Dai, B. H., Chiang, C. Y., Chiu, I. C., Pao, C. W., Lu, S. Y., et al. (2021). Rapid fabrication of high-entropy ceramic nanomaterials for catalytic reactions. *ACS Nano* 15 (7), 12324–12333. doi:10.1021/acsnano.1c04259

You, J., Yao, R., Ji, W., Zhao, Y., and Wang, Z. (2022). Research of high entropy alloys as electrocatalyst for oxygen evolution reaction. *J. Alloys Compd.* 908, 164669. doi:10.1016/J.JALLCOM.2022.164669

Zhang, Y., Wang, D., Wang, S., Zhang, Y., Wang, D., and Wang, S. (2022). High-entropy alloys for electrocatalysis: Design, characterization, and applications. *Small* 18 (7), 2104339. doi:10.1002/SMLL.202104339